Journal of Materials Chemistry A

Accepted Manuscript

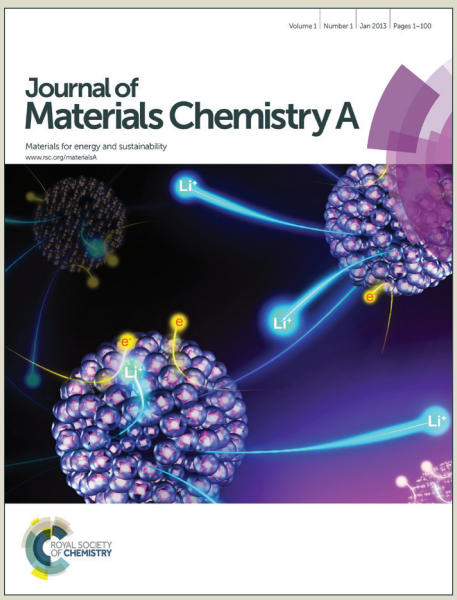

ROYAL SOCIETY OF CHEMISTRY

www.rsc.org/materialsA

Journal of Material Chemistry A RSCPublishing

ARTICLE

$Co_xMn_{3-x}O_4$ Hollow Octahedron: Synthesis, Growth Mechanism, and their Application for High-Performance Supercapacitors

Cite this: DOI: 10.1039/x0xx00000x

Received 00th January 2012,
Accepted 00th January 2012

DOI: 10.1039/x0xx00000x

www.rsc.org/

Huang Xiaomin,[a] Wang long, [d] Cao Xia,[a,b*] Yu Han,[a] Caizhen Gao,[a] Ying Xu[a] and Wang Ning [a,c*]

$Co_xMn_{3-x}O_4$ nanorod and hollow octahedron have been fabricated through a simple hydrothermal method without using any template or surfactant. Growth mechanism is studied by characterizing the intermediate products during the phase transformation. In this strategy, MnO_2 nanowire serves as the main precursor for the subsequent formation of $Co_xMn_{3-x}O_4$ nanomaterials. A merged dissolution-recrystallization and Kirkendall effect mechanism has been proposed based on SEM, TEM and XRD characterization of the intermediate. Enhanced specific capacitance (266.84 $F \cdot g^{-1}$ at 5$mV \cdot s^{-1}$), good cycle stability (remaining 80.214% after 1000 cycles) are observed in aqueous electrolytes, which should be ascribed to the high charge accommodation, small ion-transport resistance, and good electric conductivity.

1 Introduction

Due to increasing demand for energy and depletion of fossil fuels, the development of high-efficient energy storage devices attracted considerable attention from scientific and technological researchers.[1-3] Implementation of renewable energy sources, such as solar and wind energy have partially alleviated the pressure on energy demand. Supercapacitors (SCs), also known as electrochemical capacitors, is considered to be a golden storage device that could bridge the gap between batteries and conventional capacitors due to its high power density, long cycle life, fast charging efficiency, and environmental friendliness.[4-7]

Among the material of electrodes with high energy and power densities, Ruthenium oxide (RuO_2) has been the most extensively studied candidate with remarkably high specific capacitance, good proton conductivity, excellent electrochemical reversibility, high rate capability, and long cycle life. However, lacking of abundance, high prices and environmental harmfulness have made it necessary to find alternatives for practical applications. Manganese oxides have excellent physical and chemical properties under ambient conditions. In particular the rich polymorphism and structural flexibility of these compounds have allowed it a good candidate for supercapacitors because of its easy access, low cost, and environmentally harmlessness. [8] Nevertheless, the poor electrical conductivity and grave degradation greatly restrained the realization of their high theoretical capacitances (a theoretical capacity up to 1300 $F \cdot g^{-1}$), especially at high charge/discharge rates in electrochemical cycling, which restricts the research speed of manganese oxides. [9]

The fast development of multidimensional nanomaterials of controllable size, composition, and structure has opened up enormous possibilities for engineering electrode material with enhanced performance. For example, hollow micro/nano-structured materials have been considered as ideal platforms for application in electrochemical energy storage and because of

their novel interior geometry and shell functionality. [10-14] This kind of structure increased the contact area between electrolyte and active material, and reduced transport lengths for both mass and charge transport. As a result, much effort has been given to synthesize MnO_2-based hollow materials and to develop a rational design to maximize their electrochemically active sites for redox reactions through obtaining "opened" structures to further increase their energy storage density.[15-17]

Meanwhile, the critical role that impurities/dopants play has stimulated research on the creation of highly conducting nanocrystals. [18-21] Because impurities can be used to alter the properties of nanoscale materials in desirable and controllable ways, doped nanocrystals can address key problems in applications from solar cells to bio-imaging. Highly functional mixed oxide nanocrystals will require improving synthetic control over dopant incorporation, optimizing their concentrations, and investigating the phenomena that emerge. However, to the best of our knowledge, the hollow structured mixed manganese oxides have not been used so far as electrode materials for supercapacitors.

In this work, a facile template-free method was developed to synthesis hollow manganese oxide nanomaterial with tunable morphologies and compositions. Analysis of the intermediate products proved that hydrothermal treating the Co-adsorbed MnO_2 nanowire produced $Co_xMn_{3-x}O_4$ nanorods and hollow octahedron with tunable compositions. Electrochemical results show that both the energy and the power densities at high rate are greatly improved when the doped manganese oxides are used as the supercapacitor electrode material.

2 Experimental

2.1 chemicals

All reagents, unless otherwise stated, were purchase from Sinopharm Chemical Reagent Beijing Co. Ltd and used as received without further purification. Deionized water from a Milli-Q system was used throughout the experiments.

2.2 Material Synthesis

For the synthesis of cobalt doped MnO_2 nanowires, $MnCl_2{\cdot}4H_2O$ (0.162g) and $CoCl_2{\cdot}6H_2O$ (0.0685g) were first dissolved in 30 mL of isopropanol with ultrasonication for 30 minutes. After the bright blue solution was heated to 83 °C in circulating water condenser with vigorous stirring, 3 mL of $KMnO_4$water solution (containing 0.09 g of $KMnO_4$) was added rapidly. After refluxing for 30 minutes, the mixed product (Intermediate I) was centrifuged, washed with water and ethanol for several times. MnO_2 nanowires was also prepared in a similar way except the addition of $CoCl_2{\cdot}6H_2O$. For the synthesis of $Co_xMn_{3-x}O_4$ nanorod and hollow octahedron, the black slurry in the flask (Intermediate I) was transferred into 50 mL Teflon-lined stainless steel autoclave and kept at 200 °C for 2.5 and 5 h, respectively. After cooled to room temperature, the product was washed several times by centrifugation.

2.3 Characterization.

High-resolution transmission electron microscopy (HRTEM) images were obtained using a JEM-2010F transmission electron microscope at an acceleration voltage of 200 kV. Scanning electron microscopy (SEM) images were obtained by employing a Hitachi S4800 cold field emission scanning electron microscope (CFE-SEM). X-ray powder diffraction (XRD) pattern of the samples was collected by a Rigaku X-ray diffractometer (Rigaku Goniometer PMG-A2, CN2155D2, wavelength = 0.15147 nm) with Cu Kα radiation.

2.4 Electrochemical measurements.

All electrochemical experiments were carried out at room temperature, using a single compartment, three-electrode cell. An Ag/AgCl electrode was used as the reference electrode, and a Pt wire as the auxiliary electrode. The working electrode was prepared by mixing the 80 wt% of electro-active material, 10 wt% of carbon black, and 10 wt% of Polytetrafluoroethylene emulsion (10%) to obtain a well-dispersed ink samples, then painted on the nickel foam (1 cm^2) and dried at 60°C for 12 h. Then all electrodes pressed into flakes under 10 MPa.

3 Results and Discussion

3.1 Structural Characterization

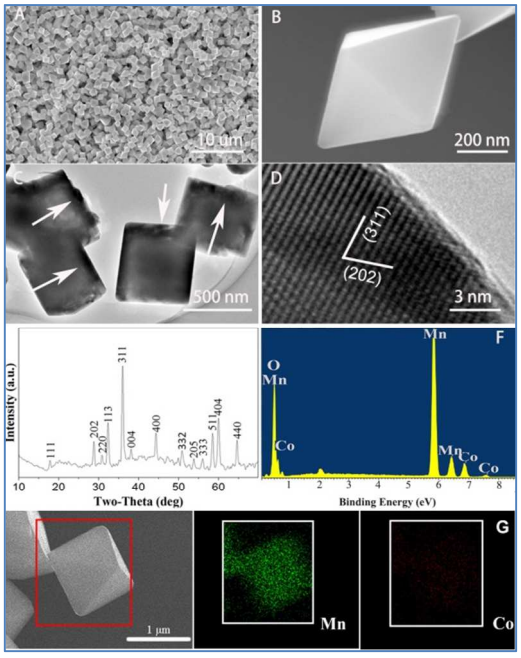

Figure 1 (A-B) SEM images of $Co_{0.4}Mn_{2.6}O_4$ octahedrons with different magnifications. (C) TEM and (D) HRTEM image of $Co_{0.4}Mn_{2.6}O_4$ octahedrons. (E) XRD pattern, and (F) EDS spectra of the $Co_{0.4}Mn_{2.6}O_4$ octahedrons. (G) EDS mapping of the $Co_{0.4}Mn_{2.6}O_4$ octahedrons.

SEM images (Figs. 1A-B) show that octahedral manganese oxide particles are synthesized on a large scale and with high uniformity. The octahedrons are enclosed by well-organized facets with average edge length of about 400 nm and elongated

<001> axe of about 800 nm. Detailed structural information is given by TEM and HRTEM images (Figs. 1C-D). The sharp contrast difference between the center and edge proves their hollow nature with a wall thickness of about 30 to 50 nm. HRTEM image (Fig. 1D) indicates a typical tetragonal lattice structure, and the marked lattice fringes with the spacing of 0.55 and 0.27 nm correspond to the (202) and (311) lattice planes. Figure 1E shows the typical XRD pattern of $Co_xMn_{3-x}O_4$. All the diffraction peaks and the high intensity of these peaks indicated the high crystallinity and purity of the $Co_xMn_{3-x}O_4$ product (JCPDS: 18-0410). The energy-dispersive spectrometry (EDS, Figs. 1F-G) result represents an averaged atomic percentage of Co of about 5.7% ($Co_{0.4}Mn_{2.6}O_4$), which can be varied conveniently from 3.8% to 20.6% by changing the precursory cobalt concentrations.

3.2 Growth Mechanism

It has been well reported that the growth of nanocrystals is rooted in surface energies. The surface energies are usually associated with crystallographic planes and different in a sequence of $\gamma\{111\} > \gamma\{100\} > \gamma\{110\}$. However, it has also been found facet-matching may be another driving force for the formation of nanowalls and nanodisks. [22-25] Here controlled experiments were carried out to investigate the formation of such hollow octahedrons.

As can be noted from the first step of the synthesis procedure, only $MnCl_2$, $KMnO_4$ and $CoCl_2$ were dissolved and heated at 83 °C and brown precipitation was obtained. SEM observation proved that ultrathin nanowires were synthesized without using any surfactant (Fig. 2A). XRD characterizations demonstrated the pure phase of MnO_2 (JCPDF no. 44-0141) (Fig. 2F), which means that the following chemical reaction was employed.

$$3MnCl_2 + 2KMnO_4 + 2H_2O \rightarrow 5MnO_2 \downarrow + 2H_2SO_4 \qquad (1)$$

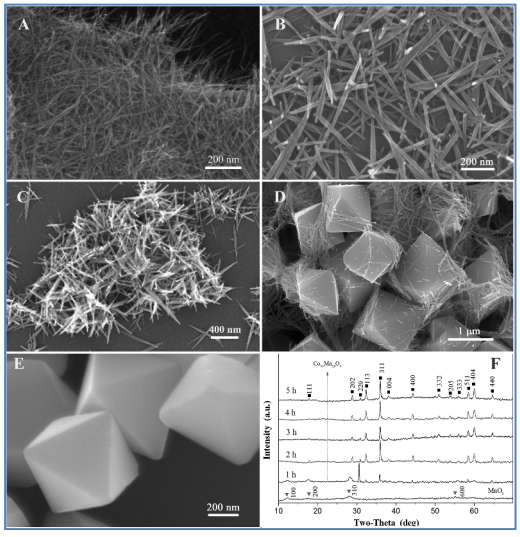

Figure 2 (A) SEM images of products after step I; (B) products of step II, 1 h; (C) products after step II, 2 h; (D) step II, 4 h; (E) step II, 5 h; (F) Comparison of XRD patterns of the product at different reaction time.

Theoretically the Gibbs free energy change (2269.2 $kJ \cdot mol^{-1}$) represents a strong tendency for this reaction to progress towards completion. The formation of nanowires is in fact of the transformation of manganese hydroxide to oxide, a process that has been well discussed in many publications for the same or similar metal alkoxides. [22-25] That is, through the formation of Mn-O covalent and Mn-OH coordination bonds, the manganese hydroxide tended to form longer chains and further to one-dimensional nanowires through van der Waals interaction as well as oxygen-bridge. [19, 26] Thus the MnO_2 nanowires acted as the original material sources for subsequent hydrothermal reactions. In this step, cobalt ion is just adsorbed by the resulted MnO_2 nanowires and doesn't affect either the formation of MnO_2, considering the Gibbs free energy change.

In the following hydrothermal step, the morphology has changed dramatically from one dimensional nanowire to hollow structured octahedrons, which should be ascribed to the dissolution-recrystallization effect under the high reaction temperature and pressure (Figs. 2B-E). It has been reported the solvothermal reaction can not only promote dissolution of oxide precursor, but also help to replace hydroxyl groups (OH^-) for oxygen (O^{2-}) and in parallel to induce cationic substitutions. Thus the solubility of the manganese precursor (MnO_2 nanowire) appears to play also an important role for orienting the stabilization of a stable structural form. Here the stabilization of different structural forms can help to form a mixed oxide via the following reactions (equation 2).

$$6MnO_2 + 3(CH_3)_2CHOH \xrightarrow{Hydrothermal} 2Mn_3O_4 + 3(CH_3)_2CO + 3H_2O \qquad (2)$$

$$xCo^{2+} + (3-x)MnO_2 \xrightarrow{Hydrothermal} Co_xMn_{3-x}O_4 \qquad (3)$$

The MnO_2 nanowires are first transformed to short $Co_xMn_{3-x}O_4$ nanorods with typical diameters of 20 to 50 nm and lengths of 200 nm to 1μm (Figs. 2B), which were then assembled with each other and formed bundle-like aggregates (Fig. 2C). When the reaction further progresses, these shortened nanorods tended to automatically agglomerated together. The obvious dissolution-recrystallization process even caused an interpenetration prototype of octahedrons with a certain angle and contact point, which eventually recrystallized into highly ordered octahedrons (Figs. 2D-E). The phase transformation is also proved by the XRD patterns shown in Fig 2F. The MnO_2 phase began to diminish with the increase of reaction time, while the diffraction ascribed to (220) and (311) of $Co_xMn_{3-x}O_4$ are intensified gradually. It takes about 2h for the complete conversion of cobalt-adsorbed MnO_2 nanowire to $Co_xMn_{3-x}O_4$ nanorods, and 4h for the Mn_3O_4 nanorod to dissolute and recrystallized in to $Co_xMn_{3-x}O_4$ octahedron.

Another interesting issue is the formation mechanism of hollow structure under hydrothermal conditions. In the past, it has been proposed that manganese oxides develops either from an initial nanoparticle agglomerated mass under the reflux conditions, or a rolling mechanism under the hydrothermal condition. [27] To investigate the detailed formation process of hollow structure under hydrothermal conditions, the

precipitates were taken out right after the reaction time exceeds 3h. Surely the reaction does not stop immediately after the autoclave is removed from the heater owing to heat transfer; we can believe the randomly dramatized samples represent certain characteristics of the formation process.

Structural information of the as prepared $Co_xMn_{3-x}O_4$ octahedron was further disclosed by SEM and TEM (Fig. 3). The clearly observed grain boundary within the octahedron hints a mechanism analogous to void formation in the Kirkendall effect (Figs. 3B-E). [28] The two solids (Mn/Co oxides) diffuse into each other at different rates and the unfilled voids are left behind. Within the small volume of a transforming $Co_xMn_{3-x}O_4$ micro/nanocrystal, the supersaturated vacancy cloud is likely to coalesce into large pores or a single void via the following route shown by Eq. 3.

In instances of cobalt doping, significant inward cobalt transport could occur through grain boundaries or during the formation of the first few monolayers of $Co_xMn_{3-x}O_4$. It is also possible that inward relaxation of the hole occurs, due to annihilation of vacancies at a semi-coherent or incoherent manganese-cobalt interface (Figs. 3B-E). It is observed that increased cobalt concentration increased hole size and enhanced outward growth of the shell, indicating that manganese mobility rather than cobalt mobility was the driving force of formation of inner voids.

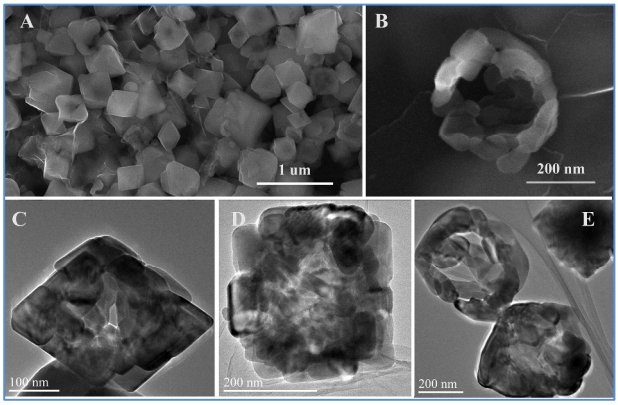

Figure 3 SEM (A) and TEM (B-E) images of the $Co_xMn_{3-x}O_4$ hollow octahedrons taken from the hydrothermally treated intermediates.

We therefore propose a possible growth mechanism for the $Co_xMn_{3-x}O_4$ hollow octahedrons, which can be divided into three stages. Firstly, MnO_2 nanowires are constructed from chains of $\{MnO_6\}$ octahedra, which are linked together to form tunnelled sequences. Under the hydrothermal conditions, dissolution–recrystallization of the MnO_2 was initiated for the formation process of $Co_xMn_{3-x}O_4$ nanorods and nano-octahedrons. With the increase of reaction time, the "Ostwald ripening" mechanism became the main factor which enabled and accelerated the transformation from nanorods to octahedrons to minimize the overall energy of the system. It can be seen that the $Co_xMn_{3-x}O_4$ nanorods are just transient intermediate products. The dissolution of nanorods and the growth of octahedrons almost occur simultaneously under the hydrothermal conditions. Further increase of the reaction time resulted in CoO-nuclei, which adsorbed on surfaces of Mn_3O_4 octahedron, forming $Co_xMn_{3-x}O_4$ layers. With the increase of reaction time, the two solids (Mn/Co oxides) diffusing into each other at different rates and the unfilled voids are left behind and coalesces into large voids due to the so called Kirkendall effect. Such process is supported by the morphology evolution at different growth stages via tuning the reaction time (Fig. 4). The truncated octahedrons is resulted from a much higher growth rate along the <100> direction than the <111> direction due to the lowest energy of the {111} surfaces.

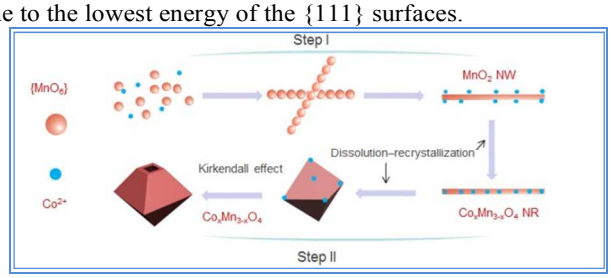

Figure 4 Schematic illustration of the growth mechanism of the $Co_xMn_{3-x}O_4$ octahedrons.

To demonstrate the use of hollow nanocrystals in energy storage, electrochemical performance of the as synthesized manganese oxides was tested by cyclic voltammetry (CV) at a scan rate of 5 $mV \cdot s^{-1}$ in the potential range of 0-1 V using 1 M Na_2SO_4 aqueous electrolyte solution (Fig. 5). The rectangular and symmetric CV curves of MnO_2, Mn_3O_4, and cobalt-adsorbed MnO_2 indicates the typical pseudocapacitive, which is sharply contrast to that of $Co_{0.4}Mn_{2.6}O_4$ and $Co_{1.4}Mn_{1.6}O_4$ (Figs. 5A-B). The lack of symmetry in the latter cases was due to the combination of double-layer and pseudocapacitive effects. In addition, the doped Co ions also make additional contributions to the total capacitance. It is interesting that performances of both $Co_{0.4}Mn_{2.6}O_4$ and $Co_{1.4}Mn_{1.6}O_4$ got significantly improved than that of pure Mn_3O_4 after the hydrothermal treatment, and $Co_{1.4}Mn_{1.6}O_4$ possesses the best performance. Since Cs is proportional to the average areas of CVs, in comparison with that of $Co_{0.4}Mn_{2.6}O_4$ and Mn_3O_4, the average area of $Co_{1.4}Mn_{1.6}O_4$ was almost covered by a straight line at different scan rates, which hints a sound cycling stability and deserves further study. In addition, there appears an anodic peak at around 0.9 V for $Co_{0.4}Mn_{2.6}O_{0.4}$, which should be ascribed to the redox reaction between Mn^{4+} and Mn^{3+}.

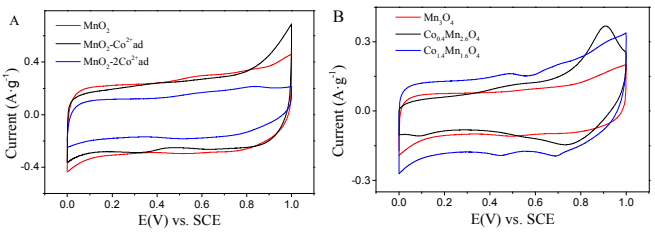

Figure 5 CVs of (A) MnO_2-xCo^{2+}ad and (B) $Co_xMn_{3-x}O_4$ at 5$mV \cdot s^{-1}$ in 1 M Na_2SO_4 solution.

Galvanostatic charge/discharge measurements were carried out in1M Na_2SO_4 between 0 and 1V at a current density of 200 $mA \cdot g^{-1}$ (Fig. 6). As illustrated in Fig. 6A, during the charging and discharging steps, the charge curve of MnO_2-Co^{2+}ad and $Co_{1.4}Mn_{1.6}O_4$ electrodes were almost symmetric to its corresponding discharge counterpart with a slight curvature, indicating the pseudocapacitive contribution along with the double layer contribution. According to the following equation

$$Cs = I \times \Delta t / (\Delta V \times m) \quad (4)$$

where I was the constant discharge current, t was the discharge time, V was the potential drop during discharge, the *Cs* values of MnO_2-Co^{2+}ad, $Co_{1.4}Mn_{1.6}O_4$ and MnO_2 nanowires can be calculated as 294, 266.84, and 236 $F \cdot g^{-1}$ from the discharge curves, respectively, which is consistent with the order indicated by the CVs. In addition, *Cs* of $Co_{1.4}Mn_{1.6}O_4$ calculated at 150, 200, 500, and 1000 $mA \cdot g^{-1}$ were 279.405, 266.84, 245.35, and 235.2 $F \cdot g^{-1}$, respectively (Fig. 6B), which means about 84.1% of Cs was retained when the current density increased from 150 to 1000 $mA \cdot g^{-1}$. This sound high power performance should be ascribed to the interior geometry and shell functionality of the hollow structure, which increased the contact area between electrolyte and active material, and reduced transport lengths for both mass and charge transport. As a result, the diffusion of ions from the electrolyte could gain full access to available pores of the electrode, leading to an almost complete insertion reaction, and therefore a higher Cs.

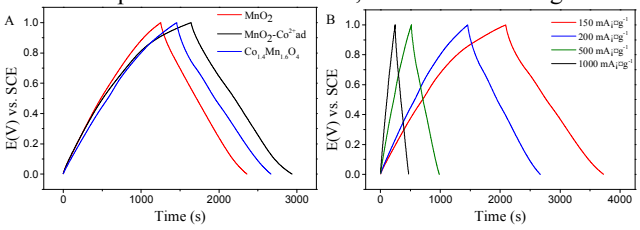

Figure 6 Galvanostatic charge/discharge curves of (A) MnO_2, MnO_2-Co^{2+}ad ions, and $Co_{1.4}Mn_{1.6}O_4$ at 200 $mA \cdot g^{-1}$ and (B) $Co_{1.4}Mn_{1.6}O_4$ at 150, 200, 500, 1000 $mA \cdot g^{-1}$.

The galvanostatic charge/discharge measurements proved that $Co_{1.4}Mn_{1.6}O_4$ hollow octahedrons possess a quite good property in spite of the decreasing trend when charge current increased to 1000 from 150 $mA \cdot g^{-1}$. To explore the potential for practical application, the current was further increased to 5000 $mA \cdot g^{-1}$ (Fig.7). The *Cs* values of $Co_{1.4}Mn_{1.6}O_4$ can be calculated as 235.2, 232.848, 232.848, 310.464, 237.352 $F \cdot g^{-1}$ corresponding to the currents of 1000, 2000, 3000, 4000, 5000 $mA \cdot g^{-1}$, respectively. The capacitances at 2000 and 3000 $mA \cdot g^{-1}$ are almost the same as that at 1000 $mA \cdot g^{-1}$, indicating a very stable performance within a wide current range. The large Cs value 310.464 $F \cdot g^{-1}$ at 4000 $mA \cdot g^{-1}$ and 237.352 $F \cdot g^{-1}$ at 5000 $mA \cdot g^{-1}$ represent a quite good high current performance for practical demands.

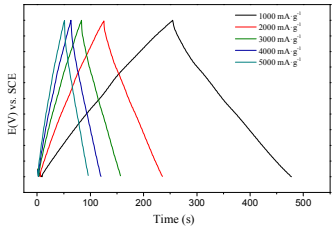

Figure 7 Galvanostatic charge/discharge curves of $Co_{1.4}Mn_{1.6}O_4$ at 1000, 2000, 3000, 4000 and 5000 $mA \cdot g^{-1}$.

The capacitance stability of $Co_{1.4}Mn_{1.6}O_4$ and MnO_2-Co^{2+}ad was investigated in the range of 0 to 1V at 200 $mA \cdot g^{-1}$ in 1 M Na_2SO_4 aqueous solution (Fig. 8). The $Co_{1.4}Mn_{1.6}O_4$ electrode retained about 80.214% (214.043 $F \cdot g^{-1}$) of initial capacitance after 1000 cycles, while that of the MnO_2-Co^{2+}ad retained only about 54.87% (161.319 $F \cdot g^{-1}$). Besides intrinsic electrochemical stability of the double-layer, we attribute the much enhanced long-time stability to the follow points. On the one hand, such porous hollow texture combines macroporous cores, mesoporous walls, and micropores together, as shown by Fig. 3. The physicochemical properties of the electrolyte in the macropores are similar to those of the bulk electrolyte with the lowest resistance. Ion-buffering reservoirs can be formed in the macropores to minimize the diffusion distances to the interior surfaces. The porous walls provide low-resistant pathways for the ions through the porous particles, and the micropores strengthen the electric-double-layer capacitance. On the other hand, the doped cobalt ions can enhance the electric conductivity, which helps to overcome the primary kinetic limits of electrochemical processes in oxide electrodes.

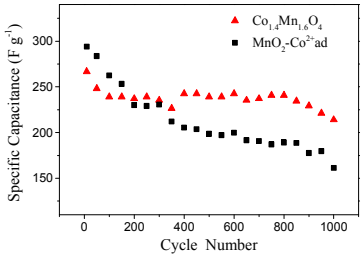

Figure 8 Cycle life of MnO_2-Co^{2+}ad and $Co_{1.4}Mn_{1.6}O_4$ at 200 $mA \cdot g^{-1}$and 1 M Na_2SO_4 solution.

Conclusions

We demonstrated that MnO_2 nanowire, $Co_xMn_{3-x}O_4$ nanorod and hollow octahedron could be fabricated through a simple hydrothermal method without using any template or surfactant. A dissolution-recrystallization mechanism has been proposed to explain the phase transformation from MnO_2 nanowire precursor, and the Kirkendall effect to account for the formation of hollow structured mixed oxides. Improved specific capacitance and good cycle stability were observed in aqueous electrolytes. We believe the sound high-power capacitance and long-term stability should be ascribed to both the intrinsic low-

resistant pathways for the ions through the porous particles as well as the enhanced electric conductivity to overcome the primary kinetic limits of electrochemical processes in oxide electrodes. We think that this concept can be extended for enhancing the performance of different electrochemical systems.

Acknowledgements

We thank the financial support from the National Natural Science Foundation of China (NSFC No. 21275102, 21173017, 21075004, and 50902007), the Program for New Century Excellent Talents in University (NCET-12-0610),The science and technology research projects from education ministry (213002A), National "Twelfth Five-Year" Plan for Science & Technology Support (No.2011BAZ01B06), Project of Thousand Talents of Chinese High-levelled Talents and the Knowledge Innovation Program of the Chinese Academy of Science (Grant No. KJCX2-YW-M13).

Notes and references

[a] Key Laboratory of Bio-Inspired Smart Interfacia Science and Technology of Ministry of Education, School of Chemistry and Environment, Beijing University of Aeronautics and Astronautics, Beijing, 100083, China. Email: wangning@buaa.edu.cn; Tel: +86 10 82316688

[b] School of Biochemical and Pharmaceutical Sciences, Capital Medical University, Beijing, 100069, China. Email: caoxia@ccmu.edu.cn

[c] Department of Chemistry, Dongguk University, Seoul 100-715, Korea.

[d] Department of Equipment Manufacture, Zhongshan Torch Polytechnic, Zhongshan, 528436, China.

Electronic Supplementary Information (ESI) available: [details of any supplementary information available should be included here]. See DOI: 10.1039/b000000x/

1. G. Wang, L. Zhang and J. Zhang, *Chem. Soc. Rev.*, 2012, **41**, 797.
2. Z. Yu, B. Duong, D. Abbitt and J. Thomas, *Adv. Mater.*, 2013, **25**, 3302-3306.
3. C. Zhou, Y. Zhang, Y. Li and J. Liu, *Nano Lett.*, 2013, **13**, 2078-2085.
4. L.-Q. Mai, F. Yang, Y.-L. Zhao, X. Xu, L. Xu and Y.-Z. Luo, *Nat. Commun.*, 2011, **2**, 381.
5. G. Yu, L. Hu, N. Liu, H. Wang, M. Vosgueritchian, Y. Yang, Y. Cui and Z. Bao, *Nano Lett.*, 2011, **11**, 4438-4442.
6. X. Lu, G. Wang, T. Zhai, M. Yu, S. Xie, Y. Ling, C. Liang, Y. Tong and Y. Li, *Nano Lett.*, 2012, **12**, 5376-5381.
7. X. Lu, M. Yu, T. Zhai, G. Wang, S. Xie, T. Liu, C. Liang, Y. Tong and Y. Li, *Nano Lett.*, 2013, **13**, 2628-2633.
8. H. Jiang, T. Zhao, C. Y. Yan, J. Ma and C. Z. Li, *Nanoscale*, 2010, **2**, 2195-2198.
9. W. Chen, Z. Fan, L. Gu, X. Bao and C. Wang, *Chem. Commun.*, 2010, **46**, 3905.
10. X. W. Lou, D. Deng, J. Y. Lee, J. Feng and L. A. Archer, *Adv. Mater.*, 2008, **20**, 258-262.
11. X. Tang, Z.-h. Liu, C. Zhang, Z. Yang and Z. Wang, *J. Power Sources*, 2009, **193**, 939-943.
12. X. Wang, X.-L. Wu, Y.-G. Guo, Y. Zhong, X. Cao, Y. Ma and J. Yao, *Adv. Funct. Mater.*, 2010, **20**, 1680-1686.
13. G. Tong, J. Guan and Q. Zhang, *Adv. Funct. Mater.*, 2013, **23**, 2406-2414.
14. J. Kang, A. Hirata, H. J. Qiu, L. Chen, X. Ge, T. Fujita and M. Chen, *Adv. Mater.*, 2014, **26**, 269-272.
15. X. W. Lou, L. A. Archer and Z. Yang, *Adv. Mater.*, 2008, **20**, 3987-4019.
16. M. C. Jing Hu, Xiaosheng Fang and Limin Wu, *Chem. Soc. Rev.*, 2011, **40**, 5472–5491.
17. W. Du, R. Liu, Y. Jiang, Q. Lu, Y. Fan and F. Gao, *J. Power Sources*, 2013, **227**, 101-105.
18. C. H. Zhang, L. Fu, N. Liu, M. H. Liu, Y. Y. Wang and Z. F. Liu, *Adv Mater*, 2011, **23**, 1020-1024.
19. Z. R. Tian, W. Tong, J. Y. Wang, N. G. Duan, V. V. Krishnan and S. L. Suib, *Science*, 1997, **276**, 926-930.
20. K. Poeppelmeier, *Science*, 2002, **295**, 1849-1849.
21. W. C. Wang, G. McCool, N. Kapur, G. Yuan, B. Shan, M. Nguyen, U. M. Graham, B. H. Davis, G. Jacobs, K. Cho and X. H. Hao, *Science*, 2012, **337**, 832-835.
22. N. Wang, X. Cao, L. He, W. Zhang, L. Guo, C. P. Chen, R. M. Wang and S. H. Yang, *J. Phys. Chem. C*, 2008, **112**, 365-369.
23. N. Wang, L. Guo, L. He, X. Cao, C. P. Chen, R. M. Wang and S. H. Yang, *Small*, 2007, **3**, 606-610.
24. C. Xia, W. Ning and G. Lin, *Sensor Actuat. B-Chem.*, 2009, **137**, 710-714.
25. X. Cao, X. L. Cai and N. Wang, *Sensor Actuat. B-Chem.*, 2011, **160**, 771-776.
26. X. Wang and Y. D. Li, *Chem-Eur J.*, 2003, **9**, 300-306.
27. X. Wang and Y. D. Li, *J. Am. Chem. Soc.*, 2002, **124**, 2880-2881.
28. Y. D. Yin, R. M. Rioux, C. K. Erdonmez, S. Hughes, G. A. Somorjai and A. P. Alivisatos, *Science*, 2004, **304**, 711-714.

Table of Contents Entry

$Co_xMn_{3-x}O_4$ hollow octahedron fabricated via merged dissolution-recrystallization and Kirkendall effect show significantly enhanced specific capacitance and cycle stability.